Journal of Materials Chemistry A

PAPER

Cite this: J. Mater. Chem. A, 2017, 5, 4058

Fe_3O_4/PANI/MnO_2 core–shell hybrids as advanced adsorbents for heavy metal ions†

Jian Zhang, Jie Han,* Minggui Wang and Rong Guo*

Received 7th December 2016
Accepted 4th January 2017

DOI: 10.1039/c6ta10499a

www.rsc.org/MaterialsA

Multifunctional magnetic adsorbents containing MnO_2 and polyaniline (PANI) with optimized adsorption properties toward heavy metal ions have been developed. In particular, Fe_3O_4 spheres were chosen as the magnetic core, followed by PANI and MnO_2 coating, realizing the formation of Fe_3O_4/PANI/MnO_2 core–shell hybrids. The as-synthesized Fe_3O_4/PANI/MnO_2 core–shell hybrids showed a hierarchical structure with a large surface area and high magnetic saturation value. In comparison with Fe_3O_4/PANI and Fe_3O_4/MnO_2 core–shell hybrids, Fe_3O_4/PANI/MnO_2 core–shell hybrids displayed the highest adsorption capacity toward heavy metal ions (including Cd(II), Zn(II), Pb(II) and Cu(II)), thanks to the integrated physical and chemical adsorption behaviors resulting from MnO_2 inorganic oxide and the PANI polymer. The developed multifunctional Fe_3O_4/PANI/MnO_2 adsorbents synthesized by a facile and economic route are believed to show high potential in environmental remediation for heavy metal removal.

Introduction

Heavy metal ions in surface water are of great concern from an environmental perspective because of their toxicity, accumulation in living beings and non-biological degradation.[1–5] As a result, it is highly desirable to remove them from wastewater before their transport and cycling into the natural environment.[6] Although various chemical and biological methods have been developed for removing heavy metal ions from contaminated water, adsorption has proven to be an effective method due to its simplicity, easy scale-up and high efficiency over a wide concentration range.[7,8] Magnetic nanoparticles, such as Fe_3O_4 and γ-F_2O_3, have been chosen as interesting adsorbents because they have high magnetic susceptibility,[9–14] which can facilitate their convenient separation from wastewater. In order to enhance the stability and acquire high adsorption capacity of adsorbents, magnetic nanoparticles are often coated with other functional materials. Among various inorganic materials for magnetic nanoparticle coating, MnO_2 has aroused increasing attention because of its high surface area, strong adsorption capacity, and good stability.[15–21]

Recently, a conducting polymer of typical polyaniline (PANI) as the organic polymer material has attracted considerable attention for removal of various pollutants from water due to its unique properties, such as easy preparation, high environmental stability, special doping mechanisms and low cost. Unlike inorganic oxides that usually follow physical adsorption toward heavy metal ions, PANI possesses functional amine and imine groups, which can guarantee massive adsorption sites for heavy metal ions resulting in extraordinary high adsorption capacity.[22–29] It is anticipated that the incorporation of PANI into MnO_2-coated magnetic nanoparticles as ternary hybrids will lead to potential advanced adsorbents, as Fe_3O_4 can guarantee magnetic separation, and physical and chemical adsorption can be both accomplished with the aid of MnO_2 and PANI. Thus, it is highly desirable to develop Fe_3O_4/PANI/MnO_2 hybrids that can further enhance the adsorption properties of pristine magnetic nanoparticles while exhibit a low-cost and environmentally benign nature. However, the incompatibility of the PANI organic conducting polymer with MnO_2 inorganic oxide means that the production of such hybrids has remained a great challenge.[30]

Herein, we reported for the first time the successful synthesis of Fe_3O_4/PANI/MnO_2 hybrids as advanced adsorbents toward heavy metal ions. As PANI can form dense coating compared to MnO_2, then PANI is firstly coated on surfaces of Fe_3O_4 nanoparticles to form Fe_3O_4/PANI core–shell hybrids, ensuring high stability especially when used in acidic solution. The introduction of mesoporous MnO_2 coating can be simply realized by addition of $KMnO_4$ into Fe_3O_4/PANI core–shell hybrids thanks to the redox activity between PANI and $KMnO_4$.[31,32] All the coating processes for PANI and MnO_2 on Fe_3O_4 can be conducted under ambient conditions through a liquid-phase (aqueous solution) synthesis route with low-cost precursors, which are critical for their practical applications. In particular, multifunctional magnetic adsorbents of Fe_3O_4/PANI/MnO_2 core–shell hybrids with a large surface area and high magnetic saturation value have been developed through a facile and economic solution route. The shell thicknesses of PANI and

School of Chemistry and Chemical Engineering, Yangzhou University, Yangzhou, Jiangsu, 225002, P. R. China. E-mail: hanjie@yzu.edu.cn; guorong@yzu.edu.cn

† Electronic supplementary information (ESI) available: TEM images of Fe_3O_4/PANI core–shell hybrids and N_2 sorption isotherms and pore size distribution of Fe_3O_4/PANI/MnO_2 core–shell hybrids. See DOI: 10.1039/c6ta10499a

MnO_2 coatings were controlled by determining the polymerization time and $KMnO_4$ amount, respectively. The adsorption processes of the Fe_3O_4/PANI/MnO_2 adsorbent toward Cd(II) ions have been studied in detail. In addition, the synergetic effect between PANI and MnO_2 has been proved to contribute to the superior adsorption capacity of Fe_3O_4/PANI/MnO_2 core–shell hybrids toward heavy metal ions (Cd(II), Zn(II), Pb(II) and Cu(II)). It is believed that Fe_3O_4/PANI/MnO_2 core–shell hybrids will find promising practical applications as highly efficient heavy metal ion adsorbents in terms of high adsorption capacity, easy availability, magnetic separation and low cost.

Experimental

Materials

Aniline was distilled under reduced pressure before use. The stock solutions of heavy metal ions were obtained from Aladdin Industrial Corporation (Cd(II), Cu(II), Zn(II) and Pb(II) standard solution). All other chemicals used were of analytical grade and used as received. The water used in this study was deionized by using a Milli-Q Plus system (Millipore, France), having 18.2 MΩ electrical resistivity.

Synthesis of Fe_3O_4/PANI/MnO_2 core–shell hybrids

The synthesis of Fe_3O_4/PANI core–shell hybrids with varied PANI shell thickness was according to our previous reports[33,34] with some modifications: 20 mg Fe_3O_4 nanoparticles as synthesized from a solvothermal method[35] were dispersed in 25 mL of deionized water, and then 100 mg PVP (K30) was added under ultrasound conditions and kept for 0.5 h to realise the surface modification of Fe_3O_4 with PVP. After that, 12 mg aniline monomers and 50 μL concentrated HCl (36–38 wt%) were added into the solution and the solution was stirred for 12 h at room temperature. The sonicator was operated at 42 kHz using a Branson 5510E-DTH apparatus. Then, 20 mL deionized water was added, and the mixture was further sonicated for 1 h at room temperature. After 1 h, an aqueous solution of ammonium peroxydisulfate (APS) oxidant (0.6 g APS in 20 mL deionized water) was added to start the oxidative polymerization under sonication at room temperature. After keeping a certain time under ultrasonic conditions, Fe_3O_4/PANI core–shell hybrids can be obtained, which were washed with deionized water and ethanol repeatedly. The particles were separated magnetically, and dissolved in 50 mL water. The resultant hybrids were denoted as Fe_3O_4/PANI(x), where x means the sonication time (min). The synthesis of Fe_3O_4/PANI/MnO_2 core–shell hybrids can be accomplished thanks to the redox activity between PANI and $KMnO_4$. In particular, 5 mL HCl aqueous solution (1 M) was added into 50 mL colloidal solution containing Fe_3O_4/PANI core–shell hybrids, followed by addition of a certain amount $KMnO_4$ solution (0.02 M). The reaction was performed under 0–5 °C under stirring for 4 h. The resulting products were washed with water and ethanol three times and dried in an oven at 70 °C overnight. Finally, the Fe_3O_4/PANI/MnO_2 core–shell hybrids were obtained. The resultant hybrids were denoted as Fe_3O_4/PANI(x)/MnO_2(y), where y means the amount of $KMnO_4$ solution added (mL).

Adsorption experiment

The adsorption capacity of heavy metal ions in aqueous solution was evaluated in a batch experiment. Aqueous solution (20 mL) containing heavy metal ions with a selected concentration range was incubated with a given amount of adsorbents at room temperature. After a desired treatment period, the metal-loaded adsorbents were magnetically separated from the solution. The supernatant was analyzed by using an Inductively Coupled Plasma Optic Emission Spectrometer (ICP-OES, Optima 7300 DV, Perkin Elmer Co., USA) or an Inductively Coupled Plasma Mass Spectrometer (ICP-MS, Elan DRC-e, Perkin Elmer Co., USA). The pH value, ionic strength, and coexisting ions (Ca^{2+}, Mg^{2+}, Cl^-, Na^+, NO_3^-, and SO_4^{2-}) of heavy metal ion solution were also adjusted to study their effects on adsorption capacity.

The uptake amount of Cd(II) ions into the adsorbent is calculated according to eqn (1) and (2), where q is the removal ratio, Q_e is the uptake capacity, C_0 is the initial metal ion concentration and C_e is the metal ion concentration at equilibrium, V is the volume of the metal ion solution, and m is the weight of the adsorbent added.

$$q = \frac{C_0 - C_e}{C_0} \times 100\% \quad (1)$$

$$Q_e = \frac{(C_0 - C_e) \times V}{m} \quad (2)$$

Characterization of Fe_3O_4/PANI/MnO_2

Morphologies of products were examined by using a scanning electron microscope (SEM, XL-30E Philip Co., Holland) and a transmission electron microscope (TEM, Tecnai-12 Philip Apparatus Co., USA). The crystal phase was analyzed by XRD using a Bruker AXS D8 ADVANCE X-ray diffractometer. The products were recorded in the 2θ range from 10° to 85.0° in steps of 0.04° with a count time of 1 s each time. Fourier-transform infrared (FTIR) spectra of products were recorded in the range of 400–4000 cm^{-1} using FTIR spectroscopy (Tensor 27, Bruker, Germany). The samples were prepared in a pellet form with spectroscopic-grade KBr. X-ray photoelectron spectroscopy (XPS) data were recorded on a Thermo ESCALAB 250 using a nonmonochromatized Al Kα X-ray (1486.6 eV) as the excitation source and choosing C 1s as the reference line. The surface area was determined from the adsorption isotherm using the multipoint Brunauer–Emmett–Teller (BET) method in the pressure P/P_0 range of 0.04–0.32. The desorption isotherm was used to determine the average pore size and distribution by the Barrett–Joyner–Halenda (BJH) method. Zeta potential measurements in aqueous solutions were performed with a Nano ZS90 Zetasizer (Malvern, UK). Magnetic measurements were carried out using a vibrating sample magnetometer (VSM, EV7, ADE, USA) with a maximum applied continuous field of 10 000 Oe at room temperature.

Results and discussion

Characterization of Fe_3O_4/PANI/MnO_2 core–shell hybrids

Scheme 1 displays the synthetic route for Fe_3O_4/PANI/MnO_2 core–shell hybrids. In order to improve the separation efficiency, superparamagnetic Fe_3O_4 nanospheres were incorporated as magnetic cores. Firstly, the PANI polymer was coated on surfaces of Fe_3O_4 nanoparticles through chemical oxidative polymerization of aniline in acidic aqueous solution using ammonium persulfate (APS) as the oxidant, leading to the formation of well-defined Fe_3O_4/PANI core–shell hybrids.[33] After addition $KMnO_4$ to colloidal solution containing Fe_3O_4/PANI core/shell hybrids, MnO_2 shells could be selectively formed on surfaces of PANI thanks to the redox activity between PANI and $KMnO_4$,[31,32] resulting in the formation of desired Fe_3O_4/PANI/MnO_2 core–shell hybrids.

In order to explore the effect of hybrid composition of Fe_3O_4/PANI/MnO_2 on the adsorption capacity toward heavy metal ions, the shell thicknesses of PANI and MnO_2 were tuned. The coating thickness of PANI shells can be well controlled by determining the polymerization time. Fig. S1† gives TEM images of Fe_3O_4/PANI core–shell hybrids with different coating thicknesses of PANI shells, where the average coating thickness increases from 5 to 20 nm with polymerization time increasing from 0.5 to 2 h. Fig. 1A shows the typical low-magnification SEM image of Fe_3O_4/PANI/MnO_2 core–shell hybrids, which reveals the uniform spherical nanostructures with a diameter of ~300 nm. The magnified SEM image as shown in Fig. 1B reveals the hierarchical nanostructure, where the surfaces are covered by numerous interconnected MnO_2 nanoflakes. The TEM image in Fig. 1C clearly evidences the uniform core–shell structure. The MnO_2 nanoflakes are measured to be 5 nm in thickness, and the coating thickness of MnO_2 shells is estimated to be 50 nm (Fig. 1D). The energy dispersive X-ray spectroscopic (EDS) elemental maps of Fe (Fig. 1E), N (Fig. 1F), Mn (Fig. 1G), and O (Fig. 1H) further confirm the successful formation of Fe_3O_4/PANI/MnO_2 core–shell hybrids.

The coating thickness of MnO_2 shells can be tuned through controlling the amount of $KMnO_4$. As given in Fig. 2A–E, the coating thickness of MnO_2 shells increases with $KMnO_4$ amount when using Fe_3O_4/PANI(1) core–shell hybrids as the starting cores. We have also prepared Fe_3O_4/PANI/MnO_2 core–shell hybrids using Fe_3O_4/PANI core–shell hybrids with varied coating thickness of PANI shells (Fig. S1†) as the starting cores. The coating thicknesses of PANI and MnO_2 shells in Fe_3O_4/PANI/MnO_2 core–shell hybrids are summarized in Fig. 2F. The weight percentages of Fe_3O_4/PANI and Fe_3O_4/PANI/MnO_2 core–shell hybrids (Fig. S2†) have been given as determined from energy dispersive spectroscopy data.

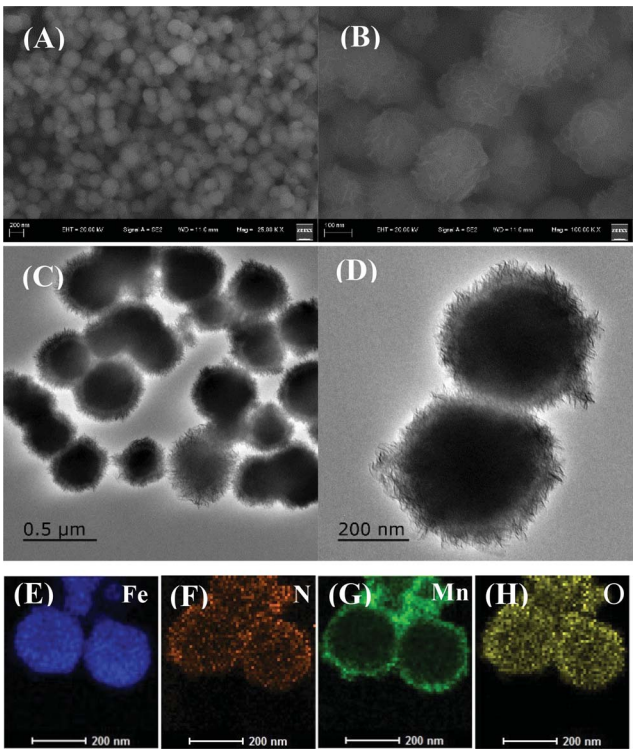

Fig. 1 (A and B) SEM and (C and D) TEM images of Fe_3O_4/PANI(1)/MnO_2(2) core–shell hybrids. (E–H) EDS elemental maps of (E) Fe, (F) N, (G) Mn and (H) O.

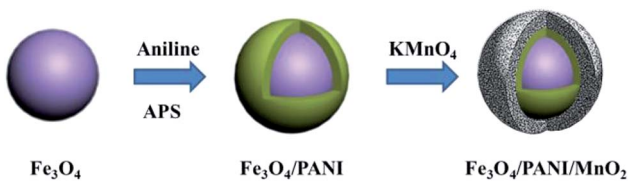

Scheme 1 Schematic representation of the synthesis processes of Fe_3O_4/PANI/MnO_2 core–shell hybrids.

The successful formation of Fe_3O_4/PANI/MnO_2 core–shell hybrids was then verified by FTIR spectra as given in Fig. 3A. As for Fe_3O_4/PANI core–shell hybrids, the strong absorption band at wavenumber 629 cm^{-1} can be ascribed to the characteristic Fe–O stretching vibration, whereas the C=C stretching deformation of quinonoid and benzenoid rings at 1576 and 1503 cm^{-1}, respectively, indicates the presence of PANI.[34] The appearance of an absorption band centered at 1297 cm^{-1} corresponding to Mn–OH stretching vibration suggests the formation of Fe_3O_4/PANI/MnO_2 hybrids. The crystalline structures were disclosed by XRD patterns as shown in Fig. 3B. The diffraction peaks at 30.1, 35.4, 43.1, 56.9 and 62.5° in Fe_3O_4/PANI core–shell hybrids corresponding to the crystal planes of (220), (311), (400), (422) and (440) of Fe_3O_4,[36] respectively, are observed. Moreover, a broad band centered at 2θ = 15–30° is also observed, which reveals that the PANI polymer is amorphous. As for Fe_3O_4/PANI/MnO_2 hybrids, no obvious diffraction peaks corresponding to MnO_2 are present, indicating that MnO_2 is also amorphous.[37] It is reasonable as the formation of MnO_2 happens under ambient conditions. Fig. S3† displays N_2 adsorption–desorption isotherms and the pore size distributions of Fe_3O_4, Fe_3O_4/PANI, and Fe_3O_4/PANI/MnO_2 core–shell hybrids.[38] The hysteresis loops in P/P_0 = 0.4–0.9 indicate the mesoporous structure of the Fe_3O_4/PANI/MnO_2 hybrids. Moreover, the appearance of the H2-type hysteresis loop suggests a porous material with relatively high uniform channel-like pores. The BET specific surface area increases from 22.94 $m^2\ g^{-1}$

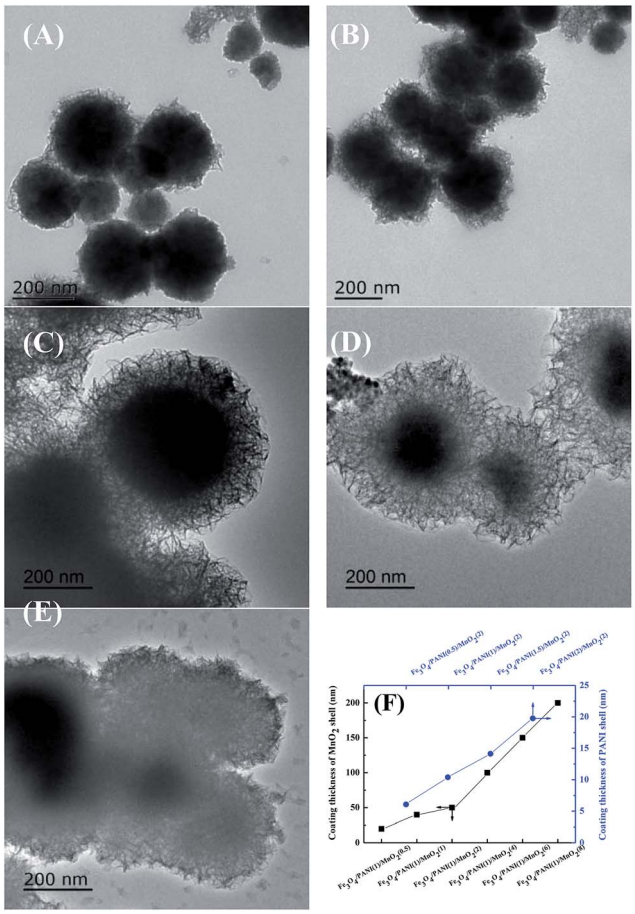

Fig. 2 TEM images of (A) Fe_3O_4/PANI(1)/MnO_2(0.5), (B) Fe_3O_4/PANI(1)/MnO_2(1), (C) Fe_3O_4/PANI(1)/MnO_2(4), (D) Fe_3O_4/PANI(1)/MnO_2(6), and (E) Fe_3O_4/PANI(1)/MnO_2(8). (F) The coating thickness of PANI and MnO_2 shells in Fe_3O_4/PANI/MnO_2 core–shell hybrids.

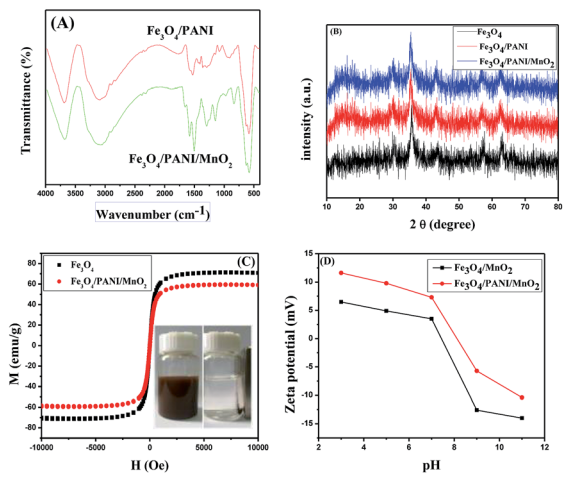

Fig. 3 (A) FTIR spectra of Fe_3O_4/PANI and Fe_3O_4/PANI/MnO_2 core–shell hybrids. (B) XRD patterns of Fe_3O_4/PANI and Fe_3O_4/PANI/MnO_2 core–shell hybrids. (C) Hysteresis loop of Fe_3O_4 and Fe_3O_4/PANI/MnO_2 core–shell hybrids. The inset shows photographs of aqueous colloidal solution of Fe_3O_4/PANI/MnO_2 core–shell hybrids (left) before and (right) after introduction of a magnet. (D) Zeta potentials of Fe_3O_4/MnO_2 and Fe_3O_4/PANI/MnO_2 as a function of pH values.

(Fe_3O_4) to 35.48 $m^2\ g^{-1}$ (Fe_3O_4/PANI), and then to 63.96 $m^2\ g^{-1}$ (Fe_3O_4/PANI/MnO_2), suggestion that the addition of PANI and MnO_2 can increase the surface area. The pore size distribution of Fe_3O_4/PANI/MnO_2 core–shell hybrids displays a single mode centered at 4.12 nm.

The magnetic properties were investigated using VSM. As shown in Fig. 3C, the magnetization curves of Fe_3O_4 and Fe_3O_4/PANI/MnO_2 core–shell hybrids show no remanence or coercivity at room temperature, indicating their superparamagnetic character. The saturation magnetization of Fe_3O_4 is 70.88 emu g^{-1}. Once conjugated with PANI and MnO_2, the saturation magnetization decreases to 59.07 emu g^{-1}. Although the saturation magnetization is lower than that of bulk magnetite (90 emu g^{-1}), it can also guarantee the easy separation of Fe_3O_4/PANI/MnO_2 core–shell hybrids from the aqueous solution with a low magnetic field gradient (inset in Fig. 3C). The zeta potentials of Fe_3O_4/MnO_2 and Fe_3O_4/PANI/MnO_2 core–shell hybrids have been measured at varied pH values (Fig. 3D), where the zeta potential of Fe_3O_4/PANI/MnO_2 hybrids is always higher than that of Fe_3O_4/MnO_2 hybrids. Results indicate that the introduction of PANI has input more positive charges in the hybrids, which resulted from its special doping mechanism. The isoelectric point for Fe_3O_4/PANI/MnO_2 was higher than that of Fe_3O_4/MnO_2, which implies that Fe_3O_4/PANI/MnO_2 hybrids are inferior in adsorption of positively charged heavy metal ions through electrostatic interactions.

Adsorption of heavy metal ions

The Fe_3O_4/PANI/MnO_2 core–shell hybrids were then applied as adsorbents to remove heavy metal ions in water. In order to verify the effect of PANI and MnO_2 coating on the heavy metal ion adsorption, Fe_3O_4, Fe_3O_4/PANI, Fe_3O_4/MnO_2 and Fe_3O_4/PANI/MnO_2 were chosen as adsorbents and the typical heavy ion of Cd(II) was selected a model adsorbate. As shown in Fig. 4, the magnetic Fe_3O_4 cores alone can only achieve 14.2% in Cd(II) removal ratio. The removal ratio can reach 44.8% for Fe_3O_4/PANI core–shell hybrids, and 65.2% for Fe_3O_4/MnO_2 core–shell

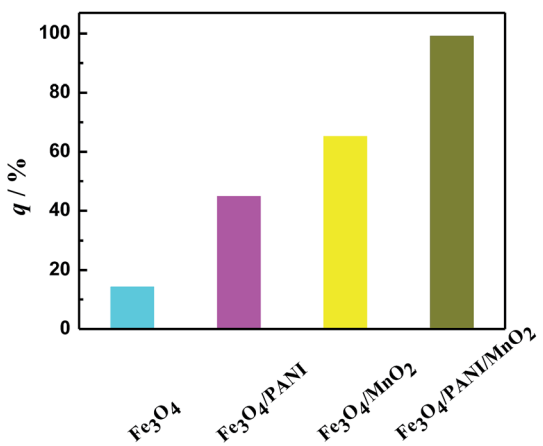

Fig. 4 Removal ratios of Cd(II) ions with Fe_3O_4, Fe_3O_4/PANI, Fe_3O_4/MnO_2, and Fe_3O_4/PANI/MnO_2 adsorbents. Adsorption conditions: [adsorbent] = 1 g L^{-1}, [Cd(II)] = 20 mg L^{-1}, pH = 6.3 ± 0.1.

hybrids. Interestingly, the removal ratio can reach up to as high as 99.1% for Fe_3O_4/PANI/MnO_2 core–shell hybrids. Results undoubtedly evidence the superior adsorption capacity of Fe_3O_4/PANI/MnO_2 adsorbents toward Cd(II) ions, which should be ascribed to the synergetic effect between PANI and MnO_2.

In order to disclose the sorption mechanism of Fe_3O_4/PANI/MnO_2 hybrids toward Cd(II), the XPS technique was applied. The binding energies of Fe 2p at 711.1 and 724.8 eV (Fig. 5A) are assigned to Fe $2p_{3/2}$ and $2p_{1/2}$, respectively. The position of the Fe $2p_{3/2}$ peak at 711.1 eV is indicative of the existence of Fe_3O_4. The binding energies of the Mn $2p_{3/2}$ and $2p_{1/2}$ states are located at 642.0 eV and 654.8 eV (Fig. 5B), respectively. This indicates a tetravalent state of Mn in the sample. As seen in Fig. 5A–C, the binding energies for Fe 2p, Mn 2p and O 1s in Fe_3O_4/PNAI/MnO_2 core–shell hybrids after Cd(II) adsorption are almost unchanged, indicating the physical adsorption of Cd(II) ions on Fe_3O_4 and MnO_2. However, as for the binding energies for C 1s (Fig. 5D) and N 1s (Fig. 5E) that come from PANI in Fe_3O_4/PANI/MnO_2 core–shell hybrids, an obvious peak shift has been distinguished after Cd(II) ion adsorption, especially for N 1s. Results suggest that Cd(II) ions may preferentially bind with N in PANI through coordination interaction. Fig. 5F displays the XPS spectra of Cd 3d for Cd(II) ions before and after sorption with Fe_3O_4/PNAI/MnO_2 core–shell hybrids,[38] where the Cd 3d standard peak position at 408.7 eV moves to 411.9 eV after sorption. However, the XPS spectrum of Cd 3d for Cd(II) ions after sorption with Fe_3O_4/MnO_2 core–shell hybrids shows no peak shift. As a result, both physical and chemical adsorption behaviors that mainly come from MnO_2 and PANI, respectively, coexist in Fe_3O_4/PANI/MnO_2 core–shell hybrids for Cd(II) ion adsorption.

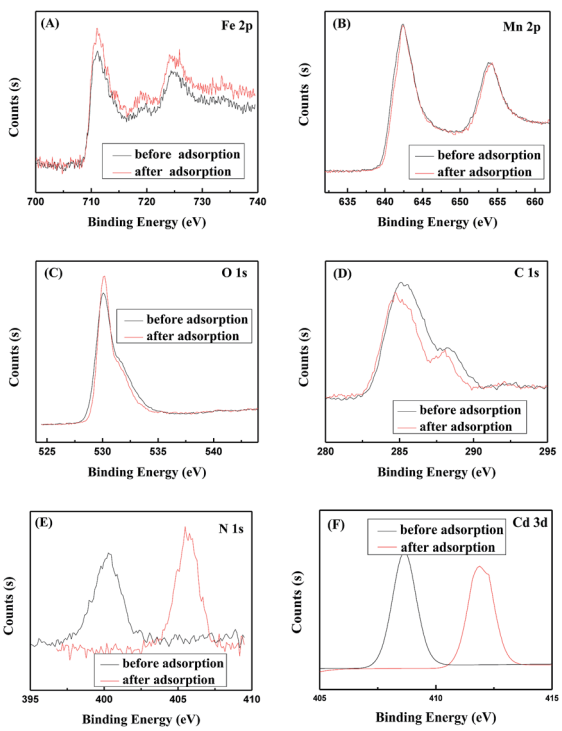

Fig. 5 XPS spectra of (A) Fe 2p, (B) Mn 2p, (C) O 1s, (D) C 1s, (E) N 1s and (F) Cd 3d.

The effect of composition of Fe_3O_4/PANI/MnO_2 core–shell hybrids for Cd(II) ion adsorption was then considered to disclose the optimized coating thickness of PANI and MnO_2 shells. As shown in Fig. 6, all the removal ratios exceed 97.0% for Fe_3O_4/PANI/MnO_2 core–shell hybrids with varied shell thickness of PANI and MnO_2, illustrating their excellent adsorption capacity which resulted from the perfect synergetic effect between PANI and MnO_2. The removal ratio increases from 97.3% to 99.3% with increasing MnO_2 coating thickness, and that increases from 98.5% to 99.2% with increasing PANI coating thickness. The optimized adsorbent composition lies in Fe_3O_4/PANI(1)/MnO_2(2) core–shell hybrids (PANI: 10 nm, MnO_2: 50 nm, Fig. 2F). As a result, Fe_3O_4/PANI(1)/MnO_2(2) core–shell hybrids were chosen as the typical adsorbents for the following adsorption studies.

The influences of pH, ionic strength, coexisting ions, and temperature on the removal ratio of Cd(II) ions were then investigated using Fe_3O_4/PANI(1)/MnO_2(2) core–shell hybrids as the model adsorbents. Fig. 7A shows that the removal ratio of Cd(II) ions increases with the pH value from 4.0 to 6.0, and then decreases with the pH value from 6.0 to 11.0. The highest removal ratio is 99.1% at pH = 6.3. As is known, there are several forms of Cd(II) ions in solution depending on the pH of solution, in which Cd^{2+} is the major form at pH < 8.0, $Cd(OH)^+$ is predominantly present at pH > 8.0, and $Cd(OH)_2$ and $Cd(OH)^{3-}$ are stable at pH > 10.0.[39] In the pH value range 4–6, the Fe_3O_4/PANI(1)/MnO_2(2) adsorbents are positively charged, and the zeta potential decreases with increasing pH (Fig. 3D). With increasing pH from 4.0 to 6.0, more protons are released from the amine/imine groups of PANI, leaving more binding sites (–N=) available for Cd(II) ion chelation.[27] As a result, the increased chemical adsorption capacity of PANI contributes to the overall adsorption capacity of Fe_3O_4/PANI(1)/MnO_2(2) adsorbents. With increasing pH value in the range 6–11, the

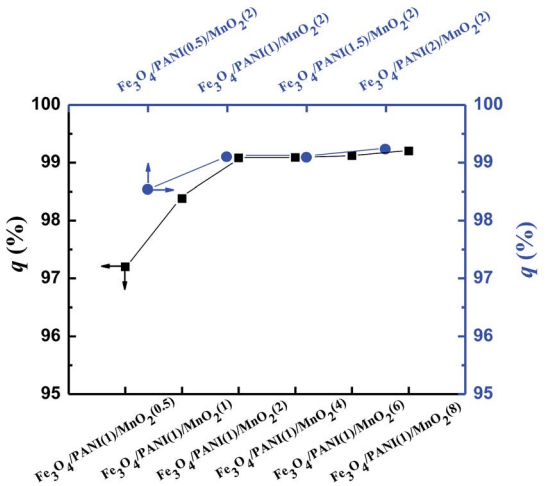

Fig. 6 Effect of coating thickness of MnO_2 and PANI shells in the Fe_3O_4/PANI/MnO_2 adsorbent on the removal ratios of Cd(II) ions. Adsorption conditions: [adsorbent] = 1 g L^{-1}, [Cd(II)] = 20 mg L^{-1}, pH = 6.3 ± 0.1.

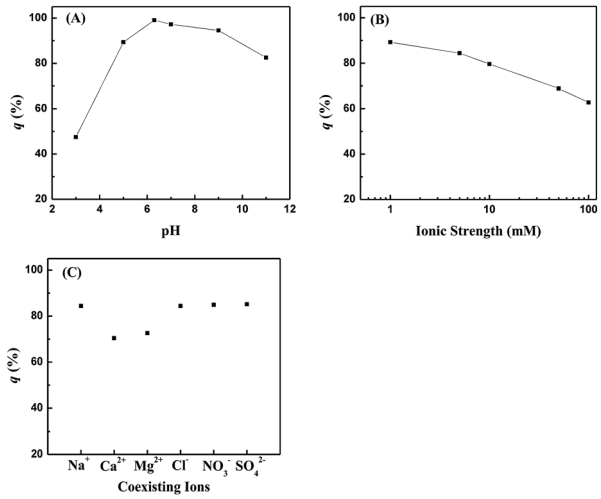

Fig. 7 Effect of (A) pH, (B) ionic strength and (C) coexisting ions on the removal ratios of Cd(II) ions with Fe_3O_4/PANI(1)/MnO_2(2) core–shell hybrids as the adsorbent. Adsorption conditions: [adsorbent] = 1 g L^{-1}, [Cd(II)] = 20 mg L^{-1}.

zeta potential of Fe_3O_4/PANI(1)/MnO_2(2) adsorbents changes from positive to negative (Fig. 3D); meanwhile, the Cd(II) ions also change from positive (Cd^{2+}) to negative ($Cd(OH)^{3-}$). As a result, the strong electrostatic repulsion between adsorbents and Cd(II) ions results in a decreased removal ratio, especially in the case of pH = 11.0. Fig. 7B shows that the removal ratio of Cd(II) ions gradually decreases from 89.5% to 62.3% as the ionic strength increases from 1 to 100 mM. It is reasonable as the electrolyte ion will compete with positively charged Cd(II) ions for the same binding sites and will influence the interfacial potential of heavy metal ions, which would in turn limit their transfer to the adsorbent surface.[16] Fig. 7C shows that the presence of coexisting cations results in a decrease in Cd(II) ion adsorption, and Ca^{2+} and Mg^{2+} ions have a greater impact than others. This can be explained in the way that such divalent cations are more competitive with Cd(II) ions for the same binding sites.

Fig. 8A gives the effect of the initial Cd(II) ion concentration on the removal ratio of Cd(II) ions into Fe_3O_4/PANI/MnO_2 core–shell hybrids. The Cd(II) ion removal ratio decreases significantly with increasing Cd(II) ion concentration, and the uptake capacity of Cd(II) ions (Q_e, eqn (1)) almost linearly increases with an increase in Cd(II) ion concentration. Two mathematical models proposed by Langmuir and Freundlich were used to describe and analyze the adsorption isotherm and equilibrium as listed in eqn (3) and (4), where Q_m is the adsorption capacity at saturation (mg g^{-1}), K_a and K_F are the equilibrium constant indicating uptake capacity, and n is the adsorption equilibrium constant. These constants were evaluated from the intercept and the slope, respectively, of the linear plots of $\frac{C_e}{Q_e}$ *versus* C_e, and log Q_e *versus* log C_e, based on experimental data through a regression analysis.

$$\frac{C_e}{Q_e} = \frac{C_e}{Q_m} + \frac{1}{K_a Q_m} \quad (3)$$

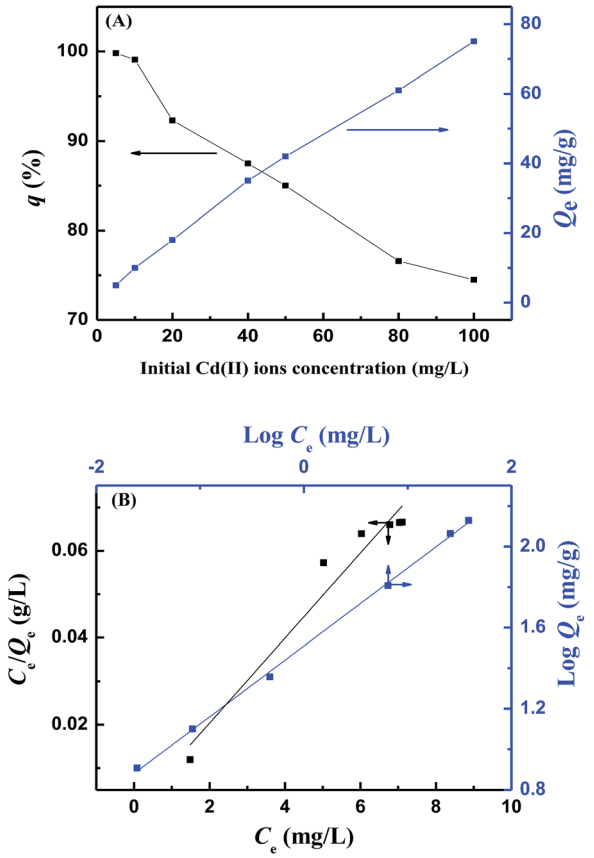

Fig. 8 (A) Effect of the initial Cd(II) ion concentration on Cd(II) ion adsorption into Fe_3O_4/PANI(1)/MnO_2(2) adsorbents. Adsorption conditions: [adsorbent] = 1 g L^{-1}, pH = 6.3 ± 0.1. (B) Langmuir and Freundlich plots of the adsorption data in the concentration range from 0 to 100 mg L^{-1}.

$$\log Q_e = \frac{1}{n}\log C_e + \log K_F \quad (4)$$

The adsorption data in the concentration range from 0 to 100 mg L^{-1} were selected to be modeled, considering that the adsorption of Cd(II) ions into Fe_3O_4/PANI(1)/MnO_2(2) core–shell hybrids basically reached equilibrium within 30 min in this concentration range. The modeled quantitative relationships between Cd(II) ion concentration and the adsorption process are shown as insets in Fig. 8B, and the calculated correction coefficients are listed in Table 1. It can be seen that the adsorption isotherm behavior of Cd(II) ions into Fe_3O_4/PANI(1)/MnO_2(2)

Table 1 Isotherm model equations for Cd(II) ion adsorption into Fe_3O_4/PANI(1)/MnO_2(2) core–shell hybrids based on the data from Fig. 8B

Mathematical mode	Equation	Correlation coefficient
Langmuir	$C_e/Q_e = 0.0065C_e + 0.0087$	0.999
Freundlich	$\log Q_e = 0.5772 \log C_e + 0.5177$	0.942

core–shell hybrids is better described by the Langmuir isotherm than the Freundlich isotherm because the Langmuir model yields a higher correction coefficient (0.999). The calculated Q_m is 154 mg g^{-1}, which is superior to that of most reported adsorbents toward heavy metal ions (Table 2). In addition, as Fe_3O_4 alone shows the lowest adsorption capacity towards Cd(II) ions (Fig. 4), and the PANI and MnO_2 coatings will block the adsorption pathway leading to deteriorated adsorption capacity of Fe_3O_4 in Fe_3O_4/PANI/MnO_2 core–shell hybrids; the adsorption capacity of Fe_3O_4 in Fe_3O_4/PANI/MnO_2 core–shell hybrids is negligible. The Q_m of Fe_3O_4/PANI/MnO_2 core–shell hybrids toward Cd(II) ions can reach as high as 428 mg g^{-1} when the quality of Fe_3O_4 in Fe_3O_4/PANI/MnO_2 is deducted just leaving PANI and MnO_2 as active materials in the calculation (Table 2).

Adsorption kinetics were studied to determine the time required for reaching equilibrium adsorption of Cd(II) ions into Fe_3O_4/PANI(1)/MnO_2(2) core–shell hybrids. Fig. 9A shows the representative plot of the adsorptive ability of Cd(II) ions into Fe_3O_4/PANI(1)/MnO_2(2) core–shell hybrids with adsorption time. It is clearly seen that the adsorption rate of Cd(II) ions into Fe_3O_4/PANI(1)/MnO_2(2) core–shell hybrids is rapid during the initial stage but becomes slow during the later adsorption time. The time required for adsorption equilibrium can be determined to be 30 min.

To gain insight into the adsorption kinetics of the removal of Cd(II) ions by Fe_3O_4/PANI(1)/MnO_2(2) core–shell hybrids, we used the experimental data in the pseudo-first-order and pseudo-second-order kinetics equations. The adsorption-rate expressions are given in eqn (5) and (6), where Q_t is the amount adsorbed (mg g^{-1}) at a certain time t, k' the rate constant of pseudo-first-order adsorption (min^{-1}), and h is the initial adsorption rate of pseudo-second-order adsorption (mg g^{-1} min^{-1}).

$$\log(Q_e - Q_t) = \log Q_e - \frac{k't}{2.303} \quad (5)$$

$$\frac{t}{Q_t} = \frac{t}{Q_e} + \frac{1}{h} \quad (6)$$

Table 2 Comparison of Q_m of Cd(II) on various adsorbents

Adsorbent	Q_m (mg g^{-1})	Reference
MnO_2-loaded resin	21.4	40
PVA/α-MnO_2–L-valine	46.3	41
MnO_2–Kaol	36.5	42
γ-MnO_2/α-MnO_2 ellipsoids	56.7[a]	43
Fe_3O_4/MnO_2	53.2	16
Fe_3O_4/PANI/MnO_2	154 (428)[a]	This work

[a] The value in the bracket is calculated when the quality of Fe_3O_4 in Fe_3O_4/PANI/MnO_2 is deducted just leaving PANI and MnO_2 as the active adsorbent. The weight ratio of Fe_3O_4 to PANI and to MnO_2 in Fe_3O_4/PANI/MnO_2 hybrids is 64 : 16 : 20 as determined from energy dispersive spectroscopy data.

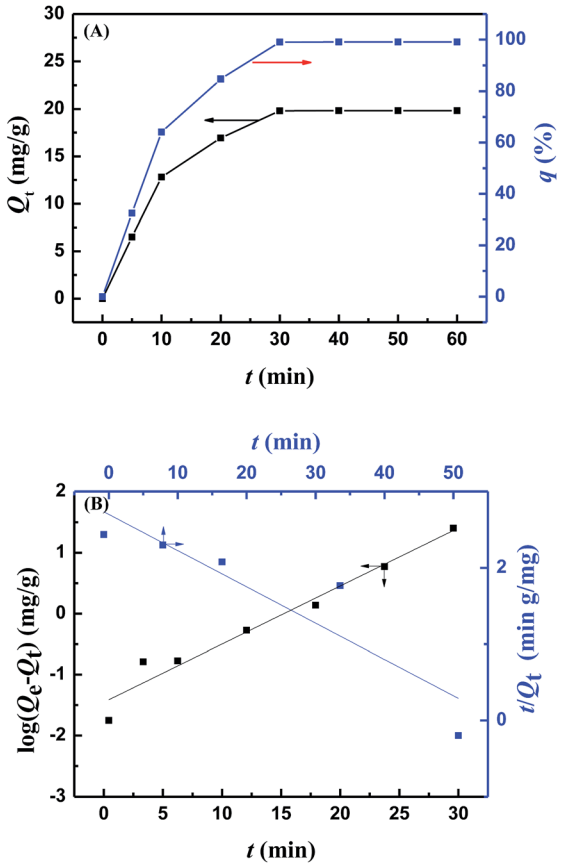

Fig. 9 (A) Effect of adsorption time on Cd(II) ion adsorption into Fe_3O_4/PANI(1)/MnO_2(2) core–shell hybrids. Adsorption conditions: [adsorbent] = 1 g L^{-1}, [Cd(II)] = 20 mg L^{-1}. pH = 6.3 ± 0.1. (B) The pseudo-first-order and pseudo-second-order plots of the adsorption data.

We used the experimental data in the pseudo-first-order and pseudo-second-order kinetic equations. The curves of $\log(Q_e - Q_t)$ and $\frac{t}{Q_t}$ *versus* t based on the data are shown in Fig. 9B. From the corresponding parameters summarized in Table 3, it is clearly seen that the adsorption kinetic behavior of Cd(II) ions into the Fe_3O_4/PANI(1)/MnO_2(2) adsorbent is more likely appropriately described by the pseudo-second-order because of a much higher correction coefficient.

In order to exploit the adaptability of the Fe_3O_4/PANI/MnO_2 adsorbent, other heavy metal ions, such as Zn(II), Pb(II) and Cu(II) ions, were also studied. Herein, Fe_3O_4, Fe_3O_4/PANI, Fe_3O_4/MnO_2 and Fe_3O_4/PANI/MnO_2 were chosen as adsorbents to verify the effect of PANI and MnO_2 coating on the heavy metal ion adsorption. As can be seen from Fig. 10, Fe_3O_4/PANI/MnO_2 core–shell hybrids show the highest uptake ratio compared to others, which is consistent with results in the case of Cd(II) ions. Then, it is believed that Fe_3O_4/PANI/MnO_2 core–shell hybrids synthesized by a simple solution route will find promising applications as highly efficient heavy metal ion adsorbents.

Table 3 Kinetic model equations for Cd(II) ion adsorption into Fe_3O_4/PANI(1)/MnO_2(2) core–shell hybrids based on the data from Fig. 9B

Mathematical mode	Equation	Correlation coefficient	Initial adsorption rate
Pseudo-first-order	$\log(Q_e - Q_t) = -0.102t + 1.672$	0.7732	0.0793 min^{-1}
Pseudo-second-order	$\frac{t}{Q_t} = 0.044t + 0.271$	0.9539	1.934 mg g^{-1} min^{-1}

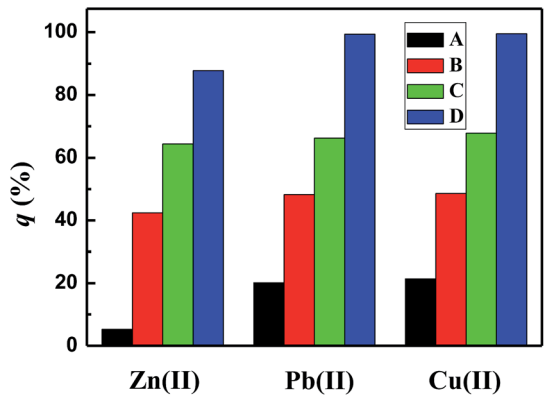

Fig. 10 Adsorption of Pb(II), Cu(II) and Zn(II) ions into different adsorbents: (A) Fe_3O_4, (B) Fe_3O_4/PANI(1), (C) Fe_3O_4/MnO_2(2), (D) Fe_3O_4/PANI(1)/MnO_2(2). Adsorption conditions: [adsorbent] = 1 g L^{-1}; [heavy metal ions] = 20 mg L^{-1}; pH = 6.3 ± 0.1.

Conclusion

Multifunctional magnetic adsorbents of Fe_3O_4/PANI/MnO_2 core–shell hybrids with a large surface area and high magnetic saturation value have been developed through a facile and economic solution route. The coating thicknesses of PANI and MnO_2 shells can be well controlled by determining the polymerization time and $KMnO_4$ amount, respectively. The adsorption data of the Fe_3O_4/PANI/MnO_2 adsorbent toward Cd(II) ion fit the Langmuir isotherm and follow pseudo-second-order reaction kinetics. In addition, the synergetic effect between PANI and MnO_2 has been proved to contribute to the superior adsorption capacity of Fe_3O_4/PANI/MnO_2 core–shell hybrids toward heavy metal ions (Cd(II), Zn(II), Pb(II) and Cu(II)). It is believed that Fe_3O_4/PANI/MnO_2 core–shell hybrids will find promising practical applications as highly efficient heavy metal ion adsorbents in terms of high adsorption capacity, easy availability, magnetic separation and low cost.

Acknowledgements

The authors gratefully acknowledge financial support from the National Natural Science Foundation of China (21673202 and 21273004), Innovation Program for Graduate Students in Universities of Jiangsu Province (No. KYZZ15_0361), Excellent Doctoral Dissertation of Yangzhou University, Qing Lan Project and the Priority Academic Program Development of Jiangsu Higher Education Institutions. We would also like to acknowledge the technical support received at the Testing Center of Yangzhou University.

Notes and references

1 J. O. Nriagu and J. M. Pacyna, *Nature*, 1988, **333**, 134–139.
2 Y. Wang, G. Ye, H. Chen, X. Hu and Z. Niu, *J. Mater. Chem. A*, 2015, **3**, 15292–15298.
3 Q. Jia, Y. C. Zhang, J. Li, Y. Chen and B. Xu, *Mater. Lett.*, 2014, **117**, 24–27.
4 Q. Zhang, S. Liu, Y. Zhang, A. Zhu and J. Li, *Mater. Lett.*, 2016, **171**, 79–82.
5 Y. Wen, S. Liu, Q. Zhang, Y. Zhang and Z. Yang, *Mater. Lett.*, 2016, **163**, 262–265.
6 Q. Qin, Q. Wang, D. Fu and J. Ma, *Chem. Eng. J.*, 2011, **172**, 68–74.
7 I. Ali, *Chem. Rev.*, 2012, **112**, 5073–5091.
8 S. Zhang, H. Gao, J. Li, Y. Huang, A. Alsaedi, T. Hayat, X. Xu and X. Wang, *J. Hazard. Mater.*, 2017, **321**, 92–102.
9 Y. Liu, G. Su, B. Zhang, G. Jiang and B. Yan, *Analyst*, 2011, **136**, 872–877.
10 H. J. Cui, J. W. Shi, B. Yuan and M. L. Fu, *J. Mater. Chem. A*, 2013, **1**, 5902–5907.
11 D. Zhang, C. Zhou, Z. Sun, L. Z. Wu, C. H. Tung and T. Zhang, *Nanoscale*, 2012, **4**, 6244–62551.
12 D. H. K. Reddy and Y. S. Yun, *Coord. Chem. Rev.*, 2016, **315**, 90–111.
13 J. Ge, Q. Zhang, T. Zhang and Y. Yin, *Angew. Chem., Int. Ed.*, 2008, **47**, 8924–8928.
14 Y. Zhao, J. Li, L. Zhao, S. Zhang, Y. Huang, X. Wu and X. Wang, *Chem. Eng. J.*, 2014, **235**, 275–283.
15 S. Zhang, Q. Fan, H. Gao, Y. Huang, X. Liu, J. Li, X. Xu and X. Wang, *J. Mater. Chem. A*, 2016, **4**, 1414–1422.
16 E. J. Kim, C. S. Lee, Y. Y. Chang and Y. E. Chang, *ACS Appl. Mater. Interfaces*, 2013, **5**, 9628–9634.
17 Z. Zhao, J. Liu, F. Cui, H. Feng and L. J. Zhang, *Mater. Chem.*, 2012, **22**, 9052–9057.
18 W. Wang, T. Jiao, Q. Zhang, X. Luo, J. Hu, Y. Chen, Q. Peng, X. Yan and B. Li, *RSC Adv.*, 2015, **5**, 56279–56285.
19 L. Tan, J. Wang, Q. Liu, Y. Sun, X. Jing, L. Liu, J. Liu and D. Song, *New J. Chem.*, 2015, **39**, 868–876.
20 J. Zhu, S. A. Baig, T. Sheng, Z. Lou, Z. Wang and X. Xu, *J. Hazard. Mater.*, 2015, **286**, 220–228.
21 R. Sahoo, M. Pradhan, A. Roy, S. Dutta, C. Ray, Y. Negishi, A. Pal and T. Pal, *Chem.–Asian J.*, 2015, **10**, 1571–1580.
22 P. S. R. Devi, S. Kumar, R. Verma and M. Sudersanan, *J. Radioanal. Nucl. Chem.*, 2006, **269**, 217–222.
23 D. Shao, G. Hou, J. Li, T. Wen, X. Ren and X. Wang, *Chem. Eng. J.*, 2014, **255**, 604–612.
24 L. Yang, S. Wu and J. P. Chen, *Ind. Eng. Chem. Res.*, 2007, **46**, 2133–2140.

25 P. A. Kumar, S. Chakraborty and M. Ray, *Chem. Eng. J.*, 2008, **141**, 130–140.
26 J. Wang, B. Deng, H. Chen, X. Wang and J. Zheng, *Environ. Sci. Technol.*, 2009, **43**, 5223–5228.
27 J. Han, J. Dai and R. Guo, *J. Colloid Interface Sci.*, 2011, **356**, 749–756.
28 J. Han, L. Wang and R. Guo, *Macromol. Rapid Commun.*, 2011, **32**, 729–735.
29 J. J. Wang, J. Jiang, B. Hu and S. H. Yu, *Adv. Funct. Mater.*, 2008, **18**, 1105–1111.
30 J. Han, M. Wang, S. Cao, P. Fang, S. Lu, R. Chen and R. Guo, *J. Mater. Chem. A*, 2013, **1**, 13197–13202.
31 J. Han, L. Li, P. Fang and R. Guo, *J. Phys. Chem. C*, 2012, **116**, 15900–15907.
32 S. Cao, N. Han, J. Han, Y. Hu, L. Fan, C. Zhou and R. Guo, *ACS Appl. Mater. Interfaces*, 2016, **8**, 6040–6050.
33 J. Han, S. Lu, C. Jin, M. Wang and R. Guo, *J. Mater. Chem. A*, 2014, **2**, 13016–13023.
34 Y. Chen, S. Lu, W. Liu and J. Han, *Colloid Polym. Sci.*, 2015, **293**, 2301–2309.
35 S. Xuan, Y. J. Wang, J. C. Yu and K. C. Leung, *Langmuir*, 2009, **25**, 11835–11843.
36 M. Ramesh, H. S. Nagaraja, M. P. Rao, S. Anandan and N. M. Huang, *Mater. Lett.*, 2016, **172**, 85–89.
37 E. Saputra, S. Muhammad, H. Sun, H. M. Ang, M. O. Tadé and S. Wang, *Appl. Catal., B*, 2013, **142–143**, 729.
38 J. Zhu, S. C. Tang, H. Xie, Y. Dai and X. K. Meng, *ACS Appl. Mater. Interfaces*, 2014, **6**, 17637–17646.
39 M. S. Berber-Mendoza, R. Leyva-Ramos, P. Alonso-Davila, J. Mendoza-Barron and P. E. Diaz-Flores, *J. Chem. Technol. Biotechnol.*, 2006, **81**, 966–973.
40 L. Dong, Z. Zhu, H. Ma, Y. Qiu and J. Zhao, *J. Environ. Sci.*, 2010, **22**, 225–229.
41 S. Mallakpour and F. Motirasoul, *RSC Adv.*, 2016, **6**, 62602–62611.
42 A. Sari and M. Tuzen, *Appl. Clay Sci.*, 2014, **88–89**, 63–72.
43 J. Cao, Q. Mao, L. Shi and Y. Qian, *J. Mater.Chem.*, 2011, **21**, 16210–16215.